Article:
Zhao, H., Zhang, X., Zhou, D. et al. (5 more authors) (2020) Collagen, polycaprolactone and attapulgite composite scaffolds for in vivo bone repair in rabbit models. Biomedical Materials, 15 (4). 045022. ISSN 1748-6041

https://doi.org/10.1088/1748-605x/ab843f

Collagen, Polycaprolactone and Attapulgite Composite Scaffolds for in vivo Bone Repair in Rabbit Models

Hongbin Zhao[1, *], Xiaoming Zhang[1], Dong Zhou[1], Yiping Weng[1], Wen Qin[1], Fang Pan[2], Songwei Lv[2], Xiubo Zhao[2, 3, *]

[1]Medical Research Centre, Changzhou Second People's Hospital Affiliated to Nanjing Medical University, Changzhou 213164, China

[2]School of Pharmaceutical Engineering and Life Science, Changzhou University, Changzhou 213164, China

[3]Department of Chemical and Biological Engineering, University of Sheffield, Sheffield S1 3JD, UK

*Authors for correspondence: (HZ) E-mail: zhao761032@163.com; (XZ) E-mail: xiubo.zhao@sheffield.ac.uk.

ToC Figure

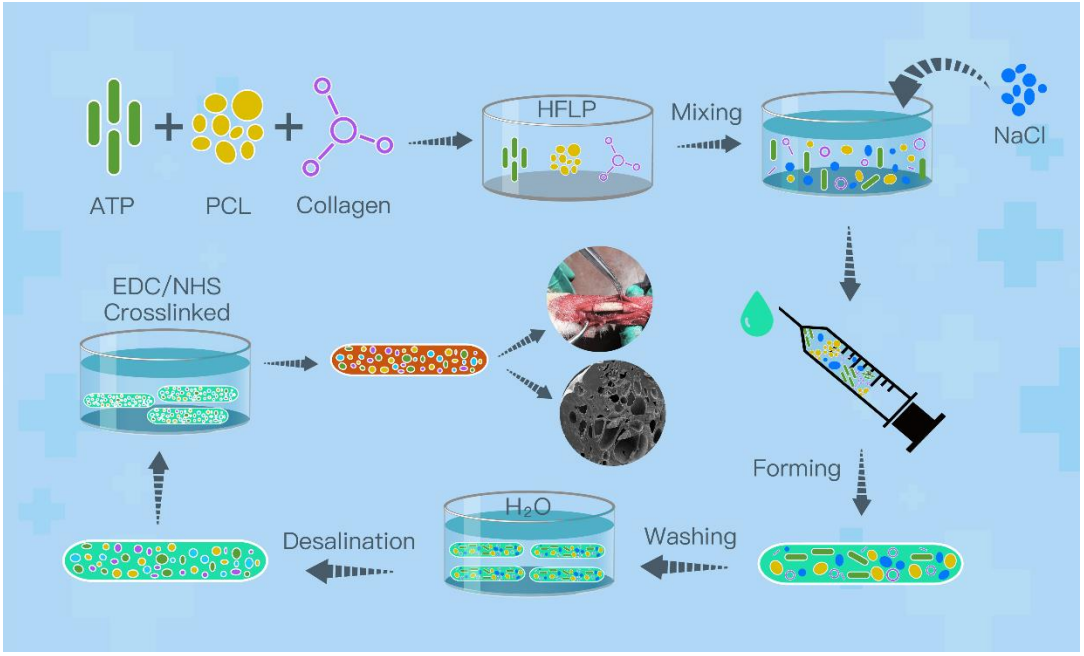

ABSTRACT

Although numerous materials have been explored as bone scaffolds, many of them are limited by their low osteoconductivity and a high biodegradability. Therefore, new materials are desired to induce bone cell proliferation and facilitate the bone formation. Attapulgite (ATP) is a hydrated silicate that exists in nature as a fibrillar clay mineral and is well known for its large specific surface area, high viscosity, and high absorption capacity, therefore has the potential to be a new type of bone repair material due to its unique physicochemical properties. In this study, composite scaffolds composed of collagen/polycaprolactone/attapulgite (CPA) or collagen/polycaprolactone (CP) were fabricated through a salt-leaching method. The morphology, composition, microstructure, physical and mechanical characteristics of the CPA and CP scaffolds were assessed. Cells from the mouse multipotent mesenchymal precursor cell line (D1 cells) were cocultured with the scaffolds, and cell adhesion, proliferation, and gene expression on the CPA and CP scaffolds were analyzed. Adult rabbits with radius defects were used to evaluate the performance of these scaffolds in repairing the bone defects over 4 to 12 weeks. The experimental results showed that the cells demonstrated excellent attachment ability on the CPA scaffolds, as well as remarkable upregulation of the levels of osteoblastic markers such as Runx2, Osterix, collagen 1, osteopontin, and osteocalcin. Furthermore, results from radiography, micro-computed tomography, histological and immunohistochemical analysis demonstrated that abundant new bones were formed on the CPA scaffolds. Ultimately, these results demonstrated that CPA composite scaffolds have excellent capability in bone tissue engineering applications and have the potential to be used as effective bone regeneration and repair scaffolds in clinical applications.

KEYWORDS: Attapulgite, Polycaprolactone, Collagen 1, Composite scaffold, Bone regeneration, Mouse multipotent mesenchymal precursor cell line D1

1. INTRODUCTION

Repairing bone defects caused by bone tumor resections, fracture defects, or chronic infection is still challenging in orthopedic practice[1-3]. Autograft is the gold-standard approach in current bone repair. However, this technique has several disadvantages, including limited supply of bone tissue, induction of new trauma, and the potential for functional damage[4, 5]. Allografts are also used clinically because of the availability in bone tissue supply, but these grafts carry the risk of infection, disease transmission, and the induction of immune response[6-8]. Advances in bone tissue engineering (BTE) have the potential to address these challenges and promote bone regeneration and repair[9-12]. However, fabricating 3D porous scaffolds for cell migration, proliferation, differentiation, and nutrient delivery is challenging.

An ideal scaffold for BTE should have i) excellent mechanical properties to enable the bone tissue remodeling; ii) excellent biocompatibility to facilitate cell attachment and proliferation; iii) appropriate biodegradability with controllable degradation and resorption rates to match the bone regeneration;

iiii) appropriate porosity for cells to attach, migrate, proliferate and deposit extracellular matrix (ECM)[1, 13]. Interconnection of pores is also required to allow the transportation of nutrients, metabolites and waste products removal[1, 14, 15].

In general, three types of bone scaffold materials have been explored in the past: bioactive ceramics, biodegradable metals and biodegradable polymers. Bioactive ceramics such as calcium phosphate (CaP) ceramics, including hydroxyapatite (HA) and tricalcium phosphate (TCP) have similar compositions to natural bone. These materials have good biocompatibility and osteoconductivity. The degradation of these materials releases ions that can enhance the cell activity and facilitate the bone repair. However, bioactive ceramics have low toughness and insufficient strength, therefore are not ideal to be used without the addition of other materials[1]. For example, HA is one of the major constituents of natural bone, accounting for 70% (by weight) of human bone[16]. HA material is biocompatible, osteoconductive, noncytotoxic, and nonimmunogenic and has a slow degradation rate[17-19]. Therefore, it has been widely used in BTE[5, 20]. However, HA is fragile, inflexible, and is difficult to model, limiting its application in bone regeneration and repair[17, 21]. Calcium phosphate (CaP) bioceramics have also been successfully applied in hard tissue regeneration as a gold standard. These bioceramics exhibit excellent biocompatibility and chemical similarity with hard tissues. Therefore, they have been extensively used in clinical repair of bone defects. Recently additive manufacturing has been employed for the fabrication of bioceramic scaffolds in addition to those traditional methods such as solvent casting, freeze drying, phase separation etc. However, due to their brittleness, poor mechanical properties and lack of other valuable trace metal ions (e.g. Si^{4+}, Sr^{2+}, and Mg^{2+}), these materials are only limited to the defects of non-load-bearing bone. To improve the mechanical properties, osteoconductivity, osteogenic ability and printability of the CaP bioceramics, inorganic and organic materials have to be incorporated with CaP bioceramics [22]. In contrast, biodegradable metals such as Mg, Zn, Fe, and their alloys have better toughness and processability than bioactive ceramics. However, biodegradable metals have a fast degradation process. The rapid degradation leads to the quick loss of mechanical integrity and stability[1]. Polymer materials are the most extensively used materials for BTE. So far, a considerable number of polymer materials such as polycaprolactone (PCL), poly-L-lactic Acid (PLLA), polyglycolic acid (PGA), polylactic acid (PLA) and poly (lactic-co-glycolic) acid (PLGA) have been developed for bone regeneration[23-29] due to their wide availability, and good mechanical properties. However, synthetic polymers are lack of bioactivity, cell affinity, and hydrophilicity[1]. Therefore, the three types of bone materials each has its advantages and disadvantages. Composite scaffolds made from the above materials combine their advantages and eliminate their shortcomes providing improved properties for BTE. Bioactive ceramics or biodegradable metals provide osteoconductivity, mechanical strength and the minerals required for BTE. Polymers can be used as binders to reinforce the mechanical property of bioactive ceramics and biodegradable metals and help model the architecture[30]. For example, chitosan has been used to make composite scaffolds with nanohydroxyapatite. It was found that the compression modulus increased with the amount of nanohydroxyapatite. The composite scaffolds were found superior in terms of cell attachment, proliferation, and morphology in relation to chitosan scaffold[31]. PLGA and PCL have also been widely used as a binder for HA in the past decades with PCL based composites attracted more attention than other synthetic polymer composites[2, 15, 31, 32]. For example, composite scaffolds made from PCL and oyster shell powder

showed Improved crystallinity and mineralization ability for BTE application[33]. PCL has also been combined with octacalcium phosphate to fabricate electrospun scaffolds for BTE[32]. Enhanced performance of osteoblast human G-292 cells on the scaffolds was observed.

While a number of excellent polymers are available, the numbers of excellent bioactive ceramics are much less. Attapulgite (ATP) is a natural clay mineral that has been used in the environmental industry as an adsorbent[34], as a decolorizing agent[35], and for catalyst support[36]. ATP is composed of SiO_2 (55.03%), Al_2O_3 (10.24%), MgO (10.49%), Fe_2O_3 (3.53%), H_2O^+ (10.13%), and H_2O^- (9.73%)[37-39], and is well known for its porosity, large specific surface area, high viscosity, and absorption ability. It possesses the physical properties as well as the minerals desired for BTE. Recently, it has been reported that electrospun ATP/PLGA nanofibers promote the differentiation of human mesenchymal stem cells into osteoblasts[40], making ATP a promising scaffold material for BTE. Combining the advantages of ATP and polymers will provide a new strategy for improved bone regeneration[38]. However, the use of ATP as bone tissue-engineering for bone repair is only emerging. Further studies are required to optimize its applications in BTE.

In this study, collagen (type 1)/polycaprolactone/attapulgite (COL1/PCL/ATP) composite scaffolds were fabricated for the BTE. Collagen is an extracellular matrix (ECM) protein of the main tissues (skin, blood vessels, and bone) [41, 42]. Scaffold manufactured with collagen has excellent biocompatibility and biodegradability[43]. Collagen is often cross-linked by physical and chemical methods using ultraviolet light, glutaraldehyde, or genipin[7, 44] to increase its mechanical properties. PCL has been widely used in regenerative medicine because of its good biocompatibility, elasticity and low immunogenic response[2, 18]. The purpose of this study was to compare a COL1/PCL/ATP (CPA) scaffold with a COL1/PCL (CP) scaffold to find out whether the addition of ATP can improve the differentiation of bone marrow–derived stroma cells into osteoblast cells, thus promoting bone regeneration. The scaffolds were made through salt leaching method as illustrated in the ToC figure and were characterized by a combination of SEM, FTIR and mechanism tests. The elemental composition, porosity, water absorption, contact angle, and degradation were investigated. Cell proliferation and morphology on the scaffolds, as well as the expression of bone regeneration related proteins such as Runx2, Osterix, alkaline phosphatase (ALP), collagen 1 (COL1), osteocalcin (OC), and osteopontin (OPN) were studied. The scaffolds were implanted into bone defects using rabbit model. Radiography, micro-CT Scan, histological and immunohistochemical staining were used to evaluate the *in vivo* bone regeneration. The current study demonstrated that CPA composite scaffolds have great potential in BTE applications.

2. MATERIALS AND METHODS

2.1 Preparation of CP and CPA Scaffolds

The porous cylindrical CP and CPA scaffolds were fabricated using a salt-leaching method[45]. Briefly, collagen type 1 (COL1) was dissolved in hexafluoro-isopropanol (HFLP) to obtain an 8% (w/v)

uniform solution. PCL polymer powder (Sigma-Aldrich, USA) was then added to the solution with magnetic stirring until a homogeneous solution was formed. The ratio of COL1: PCL was 4:1 (w/w). Various volumes of nanosized ATP (150-500 nm, Lanzhou Institute of Chemical Physics, Chinese Academy of Sciences) power and sodium chloride particles (250-500 μm, Shanghai Chemical Industry, China) were mixed with the solution to form pastes with ATP concentrations of 0% (CP scaffold; COL1:PCL:ATP mass ratio of 40:40:0), 10% (CPA-low dose [CPA-L] scaffold; COL1:PCL:ATP mass ratio of 40:40:10), and 20% (CPA-high dose [CPA-H] scaffold; COL1:PCL:ATP mass ratio of 40:40:20). The pastes were then placed into molds that were 100 mm in length and 10 mm in diameter. The molds were left in the drying oven for 6 - 8 h, and the HFLP was completely evaporated in a vacuum condition until circular cylinders had formed. The resulting highly porous CP and CPA scaffolds had lengths of 45 to 50 mm and diameter of 4 mm. The scaffolds were then placed into deionized (DI) water for 72 h to elute all the sodium chloride. Samples were then tested with 0.1 % $AgNO_3$ to conform the complete removal of NaCl.

EDC/NHS (in ethanol: water at 80:20 v/v) were used to crosslink the CP and CPA scaffolds. The air-dried scaffolds were placed in 250 mM EDC/NHS solution for 24 h at room temperature before rinsing 3 times with DI water to remove the residual EDC/NHS. After which the scaffolds were dried at room temperature. Each scaffold was cut with a surgical knife blade to 4 mm in diameter and 15 mm in length, sealed, and sterilized with Co^{60}.

2.2 Scanning Electron Microscopy

Attapulgite (ATP): The morphology and mineral content of the ATP were investigated using the scanning electron microscopy (SEM, Hitachi S-3400N system, Japan). ATP was deposited onto a carbon-coated copper grid and coated with gold for 1 h before observation. Six samples were tested with 3 times for each sample.

CP and CPA Scaffolds: SEM (JHitachi S 3400N, Japan) was used to observe the interconnected porous structure and composition of the scaffolds. Before observation, scaffolds stored in 100% ethanol were dried by supercritical carbon dioxide.

2.3 Water Absorption, Porosity, Contact Angles, and Degradation of Scaffolds

The water absorption capacities of the CP and CPA scaffolds were determined by swelling the scaffolds in 0.2 M PBS at 37°C (pH = 7.4). The scaffolds were cut into 10 mm in length and 4 mm in diameter, and separately immersed into 0.2 M PBS solution for 5 min and then for 1, 2, 3, 4, 5, 6, 24, 48, and 72 h. The water in each scaffold was then removed and weighed. The water absorption ratio was obtained with the following equation:

$$\textit{Water absorption ratio (\%)} = \frac{W_H - W_D}{W_D} \times 100\%$$

where W_H is the weight of the soaked scaffold and W_D is the weight of the dry scaffold.

For assessment of scaffold porosity, cylindrical samples were cut into 2 mm in length and 4 mm in diameter pieces. The porosity of the scaffolds was measured based on gravimetry according to the

following equation:

$$\textit{Porosity (\%)} = \frac{M_2 - M_3 - M_S}{M_1 - M_3} \times 100\%$$

where M_1 is the initial mass of a density bottle filled with ethanol, M_s is the mass of the dry scaffold, M_2 is the mass of the scaffold submerged in absolute ethanol with the density bottle, and M_3 is the mass of the density bottle after the scaffold was gently removed.

The contact angle measurement of the scaffolds was carried out with a contact angle analyzer (FTA125, First Ten Angstroms, Portsmouth, VA, USA). The scaffolds were cut into 1 cm^2 square pieces ($N = 4$) and then placed on a testing plate. Subsequently, 0.01 mL of DI water was carefully dropped onto the test sample surface. After 10 seconds, the contact angles were recorded by video monitor.

For assessment of scaffold degradation, cylindrical samples were cut into 10 mm lengths. The samples were placed into vials containing 5 mL PBS (pH = 7.4, 0.2 M), and these vials were placed into a shaking bath (37°C) for 1 to 8 weeks. The PBS solution was exchanged weekly. The loss in mass of the scaffolds was then calculated using the following equation:

$$\textit{Weight lost (\%)} = \frac{M_0 - M_D}{M_0} \times 100\%$$

where M_0 is the initial dry weight of the scaffold and M_D is the dry weight after degradation.

2.4 Fourier transform infrared spectroscopy (FTIR)

Fourier transform infrared spectroscopy (Perkin-Elmer 1600 series, USA) was used to evaluate the functional groups of the scaffolds. Before testing, a total of 2 mg dried CP or CPA scaffold powder was mixed with 200 mg KBr and compressed into a disk. All spectra were obtained between 4000 and 400 cm^{-1} at a 4 cm^{-1} resolution with 32 scans. Six samples were examined for 3 times each.

2.5 Mechanical Testing

Before testing, the scaffolds were cut so that the gauge length and diameter of all specimens were 8 mm and 4 mm, respectively. For assessment of flexural strength, the scaffolds were tested with a 3-point bend test on an Instron 4505 universal testing machine (Instron Pty Ltd., Norwood, MA, USA) at a rate of 1 mm/min. Compressive tests were performed on dry and wet scaffold (After immersion in the 0.02 M PBS (pH=7.4) for 3 days) samples using a universal testing machine with a 1 kN load cell. Specimens were compressed to 60% of their total height at a rate of 2 mm/min to obtain the load/displacement curve. Stress-strain graphs were then drawn according to the load/deformation data.

2.6 Cell Culture and Seeding on Scaffolds

Cells from the D1 mouse multipotent mesenchymal precursor cell line (CRL-12424, ATCC, USA) were cultured in DMEM/F12 (Gibco, USA) supplemented with 10% fetal calf serum (FCS) and 1% penicillin/streptomycin at 37°C and 5% CO_2. The scaffolds were sterilized with 70% ethanol for 1 h

and then rinsed 3 times with sterile PBS before the cells were loaded. The scaffolds were soaked in the DMEM/F12 medium overnight. Cells (15 μL, approximately 1.6×10^5 cells/mL) were seeded on both sides of the scaffold with a 2 h incubation step between additional seedings. The cell-seeded scaffolds were then placed into new 24-well plates containing 1 mL of DMEM/F12 complete medium. The plates were incubated at 37°C with 5% CO_2 and were cultured for 7 to 21 days. During this period, the medium was changed twice weekly. At the desired time points, the cell-seeded scaffolds were removed from the medium and analyzed for cell adhesion, proliferation, and expression of osteoblast-related genes.

2.7 Cell Proliferation and Morphology

Cell proliferation was measured using the Cell Counting Kit-8 (CCK-8; Promega, USA). In brief, the cell- seeded scaffold was removed from the original medium and placed into new cell culture plates after 1 to 7 days of culture. A total of 1 mL of medium containing 100 μL CCK-8 was added into each well, and the plates were incubated at 37°C for 3 h. A total of 200 μL supernatant was then removed from each well to a new 96-well plate and tested for absorbance at 490 nm using a plate reader (BIOTEK, USA). Six parallel samples from each group were analyzed, and each test was run in triplicate. DMEM/F12 containing 100 μL CCK-8 was used as a control.

The microstructures of the scaffolds and the cell-seeded scaffolds were assessed using SEM (JSM-5800LV). At day 3 and 7, the cell-seeded scaffolds were fixed in 2.5% glutaraldehyde in PBS for 3 additional days. The samples were then dehydrated through a series of alcohol with different concentrations (15%, 30%, 50%, 70%, 80%, 90%, 100%) followed by drying with supercritical carbon dioxide. Samples were sputter coated with gold for 10 min before the SEM measurement. Cell morphology, attachment on scaffolds, and cell density were assessed, respectively.

2.8 Fluorescence Staining

At day 7, the cell-seeded scaffolds were rinsed in 0. 2 M PBS and fixed in 10% formaldehyde for 3 additional days. After dehydration, the scaffolds were embedded in paraffin, and 5 μm sections were used for fluorescence staining. Samples were stained with 3 μM 4',6-diamidino-2-phenylindole dihydrochloride (DAPI, Sigma, USA) for the nucleus and 10 μM phalloidin (Invitrogen Life Technologies, USA) for the F-actin filaments. The samples were then observed under a fluorescence microscope (Olympus, Japan).

2.9 Reverse Transcriptase and Quantitative Real-Time PCR

The total RNA of the cells was extracted using the Trizol reagent (Invitrogen, USA) following the manufacturer's procedure. Samples with 2 μg total RNA were reverse transcribed using the M-MLV Reverse Transcription kit with an oligo (dT) 18 primer (TaKaRa Company, Dalian, China). PCR amplification was carried out in a volume of 25 μL, which contained 200 ng cDNA, 20 μM each of the forward and reverse primers (Glyceraldehyde phosphate dehydrogenase [GAPDH], Runx2, Osterix, alkaline phosphatase [ALP], COL1, osteocalcin [OC], and osteopontin [OPN]), which were

designed using Primer 3 software, and 12.5 µL of the Power SYBR Green PCR Master Mix (TaKaRa). The real-time PCR cycling conditions comprised an initial denaturation step at 95°C for 10 min, 30 cycles of 30 seconds at 95°C for denaturation, 30 seconds at 60°C for annealing, 60 seconds at 72°C for extension, and 10 min at 72°C for a final extension. Relative gene expression was detected using a comparative Ct method (2^{-ddCt}) using the following equation[46]:

Relative gene expression = 2^{-ddCt} *(DCt sample - DCt control)*

Assays were carried out in triplicate for each gene.

2.10 Examination of Bone Regeneration in Rabbits

To assess the ability of the CPA-H and CP scaffolds to promote bone regeneration in a critical-sized defect, 15 mm rabbit radius defect model was used. male Japanese white rabbits (60 in total; 2 months old; weight: 1.5-2.0 kg) were used in the study and were divided into three groups: defect control, CP, and CPA-H. All animals were anesthetized by intravenous injection of pentobarbital sodium (0.3 mL/kg). The both radius bone was exposed with a straight incision approximately 3 cm in length along the forearm bone, and 15 mm defects were made in the bilateral radius using an electric drill. Bone debris was removed with physiologic saline irrigation. The radius defects were then implanted with CP or CPA-H scaffolds (CP and CPA-H groups), with the scaffolds fixed to the ulna using absorbable sutures. In the control group, no scaffolds were implanted in the defects. The wounds were then sutured. To prevent postoperative infections, penicillin injections (400k units) were administered once a day for 7 days. The general conditions of the rabbits (diet, activity, energy, and wound healing) were continuously monitored for 2 weeks. The following experiments were carried out at 4, 8, and 12 weeks after surgery, respectively.

2.11 Radiological Monitoring

Radiography was performed to identify new bone regeneration during the healing process. Images were captured at 4, 8, and 12 weeks after surgery using X-ray machine (Faxitron MX-20, USA). Images were obtained at 45 Kv and at 3 to 5 mAs. Evidence of callus formation and bone healing in the area of defects was also assessed.

2.12 Micro-CT Scan

After radiographic examination, the rabbits were euthanized with an overdose of pentobarbital. The soft tissues attached to the bone defects were removed and the tibias were harvested and fixed in 10% formaldehyde for 48 h. The tibias were scanned using Micro-computed tomography (micro-CT) (GE Healthcare, USA) with the following parameters: voxel resolution of 15 µm with an integration time of 300 ms, at 50 keV with 850 µA current. Micro-CT software was used to transformed into 3D images and measure the bone mineral density of new bones. 3 rabbits in each group were chose to scan at 4, 8, and 12 weeks after surgery, each sample was scanned 3 times, and the amount of bone regeneration was calculated based on the average value.

2.13 Histological and Immunohistochemical Staining

Tibias were fixed in 10% formaldehyde for 3 days and were then decalcified in 5% EDTA at room temperature (pH = 7.0) for 5 weeks. After complete decalcification, the bone specimens were dehydrated in ascending ethanol and then embedded in paraffin. The paraffin blocks were sectioned into 5 μm thicknesses, stained with H&E and Masson staining, and analyzed with a microscope (Olympus, Japan). The quantity of new bone area ratio was assessed using Image-Pro Plus 6.0 software (Media Cybernetics, Rockville, MD, USA). For immunohistochemical analysis, the sections were deparaffinized and then rehydrated by boiling them for 10 min in a sodium citrate solution. The following protocols were performed according to the manual of the immunohistochemical kit: Sections were treated with several primary antibodies: rabbit monoclonal ALP antibody (1:1000, overnight at 4°C; Abcam, USA), rabbit monoclonal COL1 (1:1000, overnight at 4°C; Abcam, USA), rabbit monoclonal type 2 collagen (COL2) (1:1000, overnight at 4°C; Abcam, USA), (1:1000, overnight at 4°C; Abcam, USA), and rabbit monoclonal OPN antibody (1:1000, overnight at 4°C; Abcam, USA); and then with a biotinylated goat anti-mouse or anti-rabbit secondary antibody for 30 minutes. Sections were stained with 3,3'-diaminobenzidine tetrahydrochloride (DAB; Sigma, USA), rinsed with PBS, dehydrated, and examined with a microscope (Olympus). All histological and immunohistochemical images were photographed digitally with a microscope and analyzed with a digital image analysis system (DXM 1200, Nikon, Japan).

2.14 Study Approval

All animal experiments in this study were approved by China's Animal Research Authority and Ethics Committee of the General Hospital of Lanzhou Military Command of the PLA. All animal studies were performed in compliance with the regulations and guidelines of the Orthopedics department of the General Hospital of Lanzhou Military Command of the PLA, and animal care was conducted according to the Association for Assessment and Accreditation of Laboratory Animal Care international (AAALAC) and Institutional Animal Care and Use Committee (IACUC) guidelines.

2.15 Statistical Analyses

All data are presented as means ± standard deviations. A two-tailed unpaired Student's t test was used to assess for significant differences between groups; P value < 0.05 was considered statistically significant. SPSS 13.0 statistical software (SPSS, USA) was used to analyze all data.

3. RESULTS

3.1 Morphology and Chemical Composition of the ATP and CPA Scaffolds

SEM measurements were carried out to reveal the morphology of the ATP, COL1/PCL (CP) and COL1/PCL/ATP (CPA) scaffolds with the data shown in Figure 1. ATP (Figure 1A) showed clusters of single rod structure with relatively smooth surfaces. The approximate length of the ATP rods was 0.2 to 1.8 μm with the diameter range from 15 to 50 nm. ATP was found composed of SiO_2 (33.7%), MgO (9.0%), Al_2O_3 (5.6%), Fe_2O_3 (4.1%), CaO (1.5%), KBr (1.3%), and Ti (0.5%) (Figure 1Ac).

Figure1B shows the SEM micrographs of CP and CPA scaffolds. The scaffolds showed porous structures, with pore sizes ranging from 250 to 500 µm, which were created by the sodium chloride particles. This porosity was beneficial for nutrient exchange and cell migration. Figure 1C shows the chemical composition of the CPA-H scaffolds. Strong signals were detected for Si, Mg, Al, and Fe, indicating the presence of ATP in the scaffolds. With an increase in ATP, Si was also increased (Figure S1), indicating the existence of an Si-containing material in the scaffolds. A strong carbon signal was also detected in the CPA scaffolds.

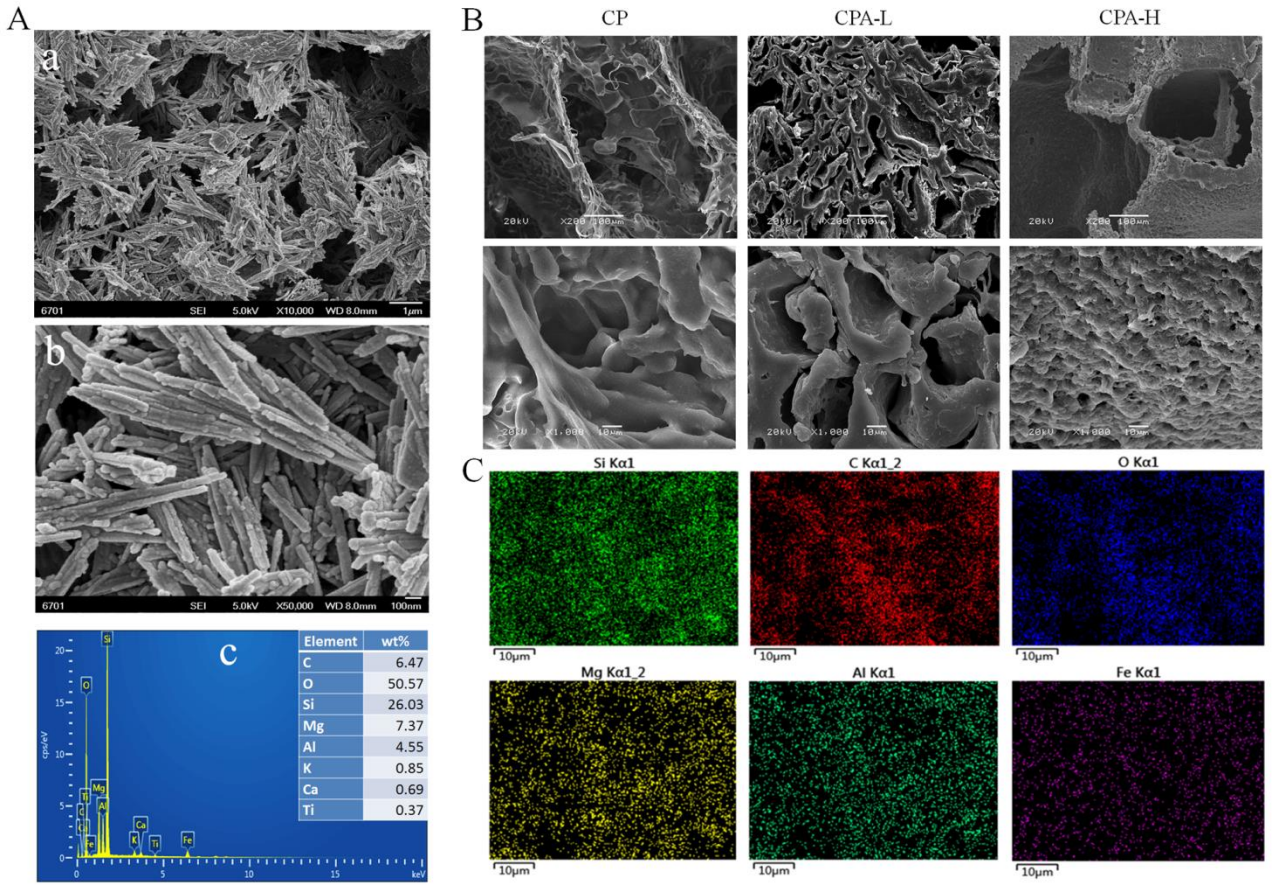

Figure 1. (A) Surface topography of attapulgite (ATP) (a & b) with the elemental composition of ATP shown in (c). (B) SEM micrographs of the surface topography of CP, CPA-low dose (CPA-L), and CPA high-dose (CPA-H) scaffolds. (C) Distribution of the elemental composition of the CPA–H scaffold.

3.2 Characterization of the scaffolds: Porosity, water absorption, contact angle, degradability, mechanical properties, and FTIR study

The CPA-H scaffold with and without cross-linking were observed under SEM. Higher porosity was observed in CPA scaffolds that were not cross-linked (Figure 2A). When the scaffold was cross-linked by EDC/NHS, the structure became more compacted (Figure 2B) with decreased porosity. However, after cross-linking, the porosity values for CP (87.7%), CPA-L (82.9%) and CPA-H (82.9%) were very similar (Figure 2C). The addition of the ATP only resulted in small decrease of the porosity. The water absorption values for the cross-linked scaffolds are shown in Figure 2D. The water

absorption values decreased from 281.7% for CP to 234.9% for CPA-L and 150.7% for CPA-H, indicating that the water absorption capacity of the scaffolds decreased with increasing ATP concentration. The was due to the fact that ATP has less water adsorption ability. The contact angles (shown in Figure 2E) of the scaffolds were 76° for CP, 57.3° for CPA-L and 42.5° for CPA-H. These data suggest that the contact angle of the scaffolds was decreased when the amount of ATP was increased. Figure 3F shows the degradability of the cross-linked scaffolds after immersion in PBS solution. After being soaked for 8 weeks, the CPA-H, CPA-L, and CP scaffolds demonstrated weight loss values of 42.6%, 47.1%, and 70.2%, respectively, suggesting that the degradability of the scaffolds was decreased when the amount of ATP was increased.

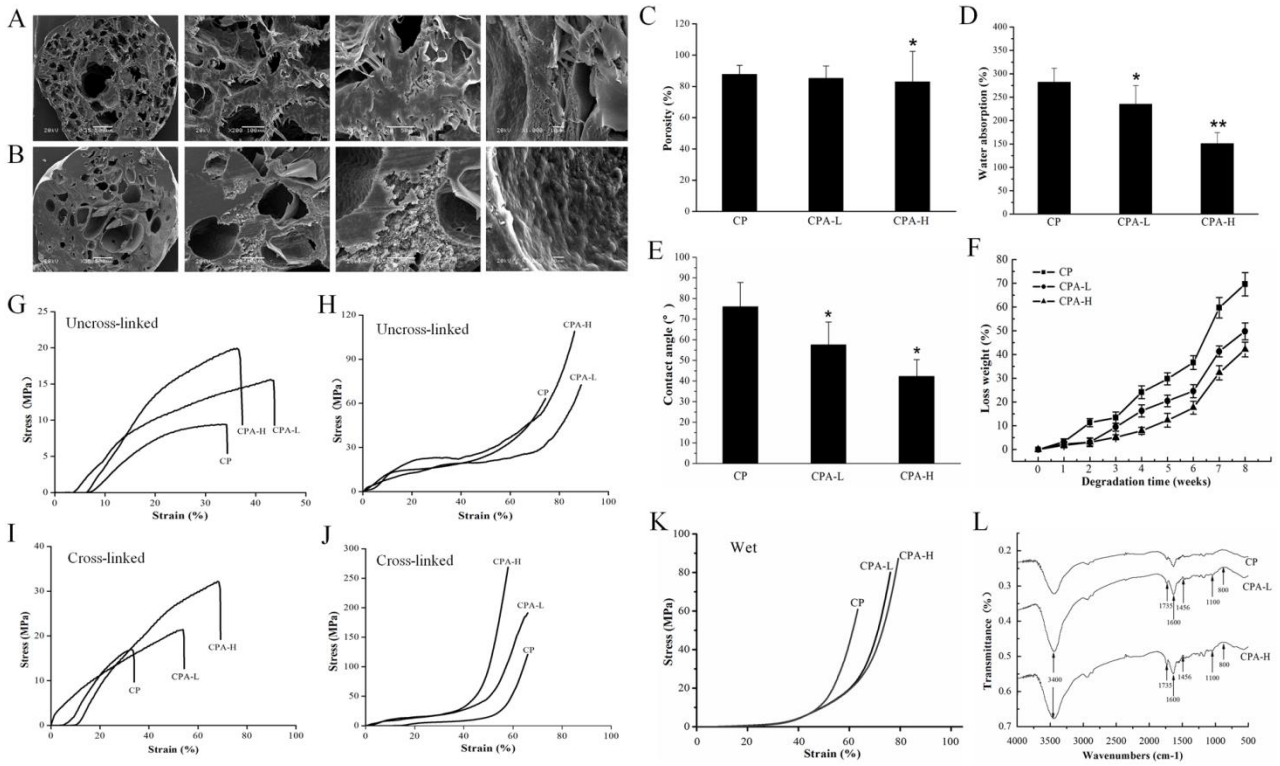

Figure 2. Characterization of the CP and CPA scaffolds. (A & B) SEM micrographs of CPA-H scaffolds with (B) and without (A) cross-linking. (C) Porosity, (D) water absorption, (E) contact angle, and (F) degradability of the CP and CPA scaffolds. (G-K) Mechanical properties of the CP and CPA scaffolds. (G & I) Stress/strain curves from the 3-point bend test of the CP and CPA scaffolds. (H & J) Stress/strain curves from the compression test of the CP and CPA scaffolds. (K) Stress/strain curves from the compression test of the CP and CPA scaffolds on wet condition. (L) FTIR spectra of the CP, CPA-L and CPA-H scaffolds. Data are shown as mean ± standard deviation (n = 4). * P < 0.05; ** P < 0.01.

The stress-strain curves from the 3-point bend test are shown in Figure 2G and 2I. The average tensile strengths of the uncross-linked CPA scaffolds were 20.0 ± 1.0 MPa for CPA-H and 15.04 ± 0.7 MPa for CPA-L, higher than the tensile strength of the uncross-linked CP scaffolds (8.2 ± 0.3 MPa) (Figure 2G). Meanwhile, the average tensile strength of the cross-linked CPA-H scaffolds was 32.6 ± 2.2 MPa, higher than the tensile strengths of the cross-linked CPA-L scaffolds (21.4 ± 1.8

MPa) and the cross-linked CP scaffolds (16.2 ± 1.4 MPa) (Figure 2I). These data demonstrated that both addition of ATP and cross-linking of the scaffolds increased the tensile strength of the scaffolds. Figure 2H and 2J show the compressive strength of the scaffolds. The average compressive strength of the uncross-linked CPA scaffolds was 109 ± 6 MPa for CPA-H and 72.5 ± 0.6 MPa for CPA-L, higher than the compressive strength of the uncross-linked CP scaffolds (65.4 ± 2.1 MPa). The average compressive strength of the cross-linked CPA-H scaffolds was 261 ± 4 MPa, higher than the compressive strengths of the cross-linked CPA-L scaffolds (192 ± 4 MPa) and the cross-linked CP scaffolds (125 ± 5 MPa). On the wet condition, the average compressive strength of the cross-linked CPA-H scaffolds was 90.3 ± 4 MPa, higher than the compressive strengths of the cross-linked CPA-L scaffolds (79.5 ± 1 MPa) and the cross-linked CP scaffolds (59.65 ± 2 MPa).These results demonstrated that both addition of ATP and cross-linking of the scaffolds increased the compressive strength of the scaffolds.

The FTIR spectra of the scaffolds are shown in Figure 2L. The spectra of the CPA scaffolds demonstrated a typical and predominantly antisymmetrical stretching vibration peak at 1100 cm^{-1}, representing the Si-O-Si bond of the CPA scaffolds. A symmetrical stretching vibration representing the Si-O vibrational peak at 800 cm^{-1} was also observed. Peaks that occurred at 3400 cm^{-1} and 1600 cm^{-1} represented amide A and amide I from collagen in both the CP and CPA scaffolds. In the CPA scaffolds, amide I and amide II appeared as peaks at 1735 cm^{-1} and 1456 cm^{-1} representing C=O and N-H stretching of the collagen polyether peaks, respectively.

3.3 Cell Morphology, Adhesion, and Proliferation on the Scaffolds

Figure 3 shows the (CRL-12424) cell morphology, adhesion, and proliferation on the scaffolds. After 3 days of culturing, a small number of cells was observed on the CP scaffolds, whereas large numbers of cells were observed on the CPA-L and CPA-H scaffolds. At day 7, the cell population density increased for all the scaffolds, and the deposition of extracellular matrix (ECM) was observed on the both CPA-L and CPA-H scaffolds. During the same time period, a very high cell density was observed on the CPA-H scaffold surface. The cells were more elongated on CPA-H scaffold surface. The pores on the scaffold were covered by the cells and ECM secreted from the cells. In addition, a crystal-like ECM structure was observed on the lower-right side of the CPA-H scaffolds (Figure 3A). Immunofluorescence staining (Figure 3B) indicated substantially higher cell numbers on the CPA scaffolds than that on the CP scaffolds at 7 days after inoculation.

CCK-8 assay was performed to evaluate the cell proliferation of CRL-10915 cells on scaffolds with the data shown in Figure 3C. No significant difference in cell proliferation was seen for the CPA and CP scaffolds at day 1. At day 3, clear differences were observed. Cell proliferation increased with the increasing amount of ATP in the scaffolds. By day 7, cell proliferation on the CPA-H scaffolds was remarkably increased when compared with cell proliferation on the CPA-L and CP scaffolds.

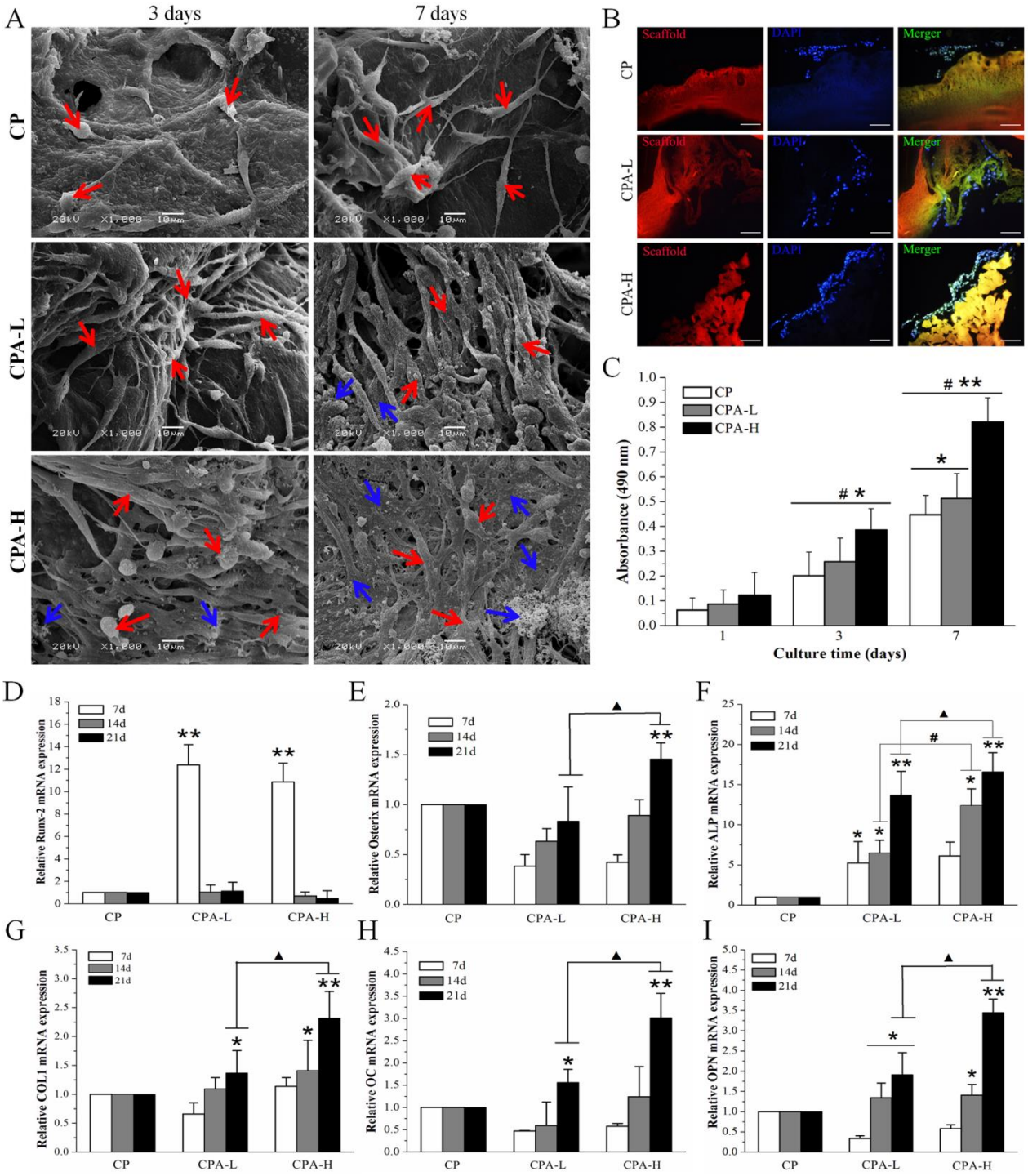

Figure 3. Adhesion, proliferation and Osteogenic differentiation of D1 cells on the CP and CPA scaffolds. (A) SEM images of cell adhesion and proliferation at 3 and 7 days on the scaffolds. (B) Immunofluorescence staining of cell adhesion and proliferation on the scaffolds at day 7. Red = scaffold; blue = nucleus; green = F-actin. (C) Cell proliferation on the scaffolds assessed by Cell Counting Kit-8 assay. (D-I) mRNA expression assays of bone tissue-specific markers: (D) Runx2, (E) Osterix, (F) alkaline phosphatase (ALP), (G) collagen type 1 (COL1), (H) osteocalcin (OC), and (I) osteopontin (OPN). Data are shown as mean ± standard deviation ($n = 3$). Red arrow= cells; Blue arrow= extracellular matrix (ECM). Scale bars = 100 μm. * $P < 0.05$; ** $P < 0.01$; # $P < 0.05$; ▲$P<0.05$.

3.4 Expression of Osteoblast Molecular Markers

Osteoblast molecular markers are important indicators for bone regeneration. Figure 3D-I show the mRNA expression of bone tissue-specific markers between 7-21 days. After 7 days of incubation, the expression level of Runx2 mRNA was notably increased in cells implanted on the CPA scaffolds versus those implanted on the CP scaffolds. The expression level of Runx2 rapidly decreased after 14 and 21 days in cells on the CPA scaffold (Figure 3D) indicating the differentiation of the multipotent mesenchymal precursor cells into osteoblasts. The mRNA expression level of Osterix (Figure 3E) of CPA-L and CPA-H scaffolds were lower than that of CP scaffolds at day 7. However, it gradually increased with time and the concentration of ATP. At day 21, the mRNA expression level of Osterix was significantly higher than that of CP and CPA-L scaffolds. Similar trends were observed for the mRNA expression levels of COL1 (Figure 3G), OPN (Figure 3H) and OC (Figure 3I). For the mRNA expression level of ALP, the expression level was low for CP scaffold, but significantly increased with time and the increased percentage of ATP (Figure 3F).

3.5 Implantation Procedure, Radiographic Examination and Micro-CT Scan

The CP and CPA-H scaffolds were implanted into 15 mm rabbit radius defect model with the implantation procedure shown in Figure 4A. X-ray experiments were performed at 4, 8, 12 weeks after implantation (Figure 4B). Postoperative radiographs demonstrated that clear defects can be observed at the implants' areas at week 4. However, some low-density developments were also observed in the bone defect areas. The bone regeneration of CPA-H is better than CPA-L and CP. At week 8, defects can still be seen in CP scaffold areas, while in CPA scaffold areas, the defects were filled in with low density new bone. At week 12, all the defects were filled in with CPA scaffolds have higher density bone. In the CPA-H group, a bone marrow cavity formed in the newly formed bone by week 12 (Figure 4B).

Figure 4C shows the Micro-CT scan results of the scaffold areas. At 4 weeks, a small amount of bone-like tissue was observed within the bone defect area in the CP scaffold group (Figure 4C). However, the tissue mineral content was markedly lower in this group than that in the CPA-H scaffold group (Figure 4D). After 8 weeks, bone-like tissue was observed in the CPA-H and CP groups, but the bone observed in the CP group was discontinuous. In addition, the tissue mineral content of the bone defect area was markedly lower in the CP group than that in the CPA-H group. A large amount of new bone-like tissue was observed in the bone defect area of the CPA-H scaffold group at 12 weeks after transplantation. The tissue mineral content was remarkably increased in the CPA-H scaffold versus the control group. The tissue mineral content showed a dose and time dependent manner (Figure 4D). The more ATP presented in the scaffolds the higher tissue mineral content was detected. The tissue mineral content also increases with postoperative time.

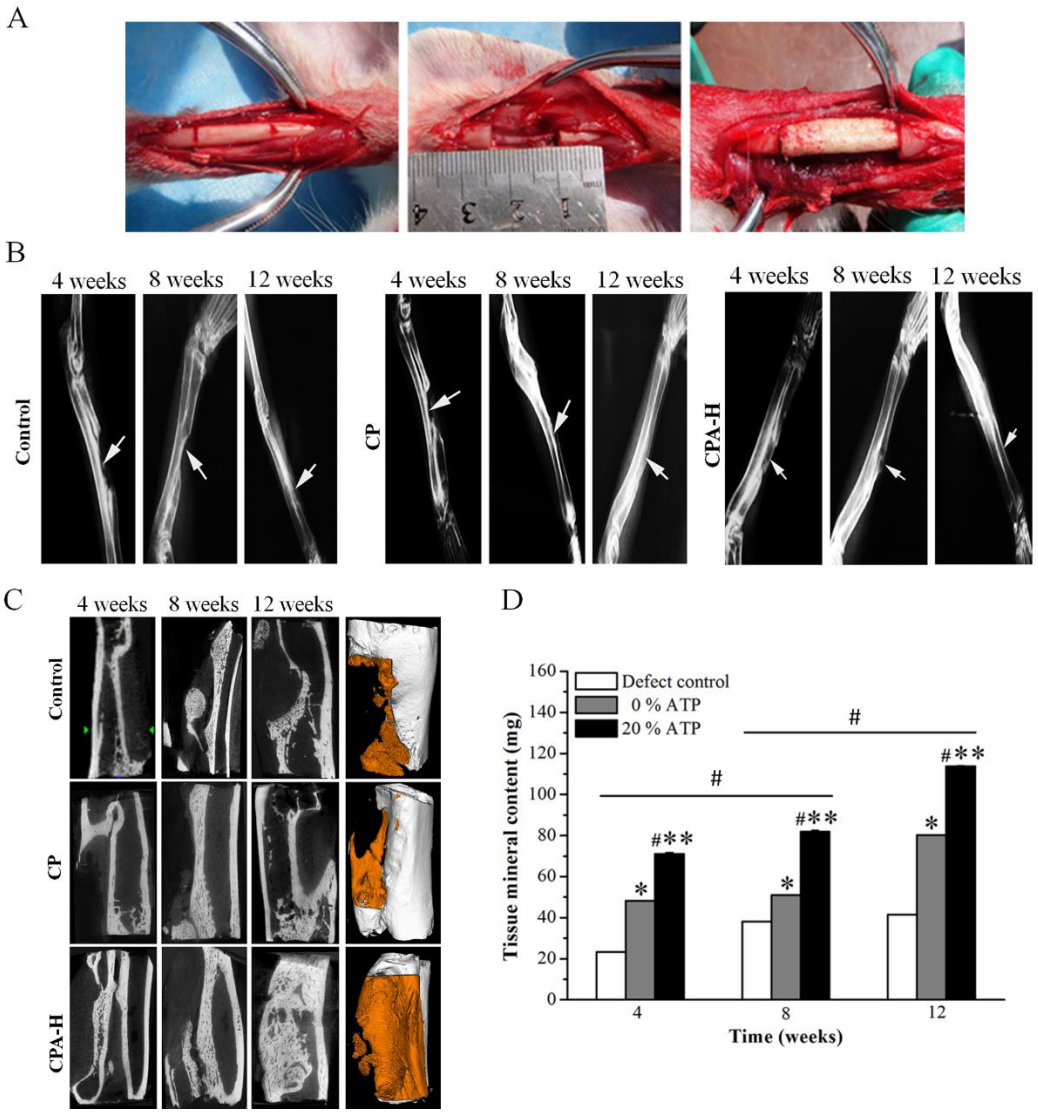

Figure 4. Implantation procedure, X-ray and micro-CT analysis of new bone. (A) Photographs showing the surgical implantation procedure for CP and CPA-H scaffolds in rabbit bone. Representative radiographs (B) and Micro-CT images (C) showing the level of regenerated bone tissue after 4-12 weeks. (D) Tissue mineral content of the regenerated bone tissue after 4-12 weeks. Data are shown as mean ± standard deviation (n = 3). CPA-H = CPA high-dose. * $P < 0.05$; ** $P < 0.01$; # $P < 0.05$; ## $P < 0.01$.

3.6 New Bone Formation Assessed by Histologic Analysis

Histologic Analysis was performed at week 4, 8, and 12 to evaluate the new bone formation with data shown in Figure 5. Four weeks after transplantation, monocytes, plasma cells, and lymphocytes were observed within all implant scaffolds. At week 8, the presence of fibrous connective tissue was seen in the control group. In the CP group, the scaffold materials partially disappeared, and more fibrous connective tissue grew into the scaffolds, indicating the degradation of the scaffolds was faster than the desired degradation rate. In contrast, new bone was observed in the CPA-H scaffold

group. At week 12, most of the area of bone defect was covered by fibrous connective tissue in the control group, indicating that new bone had not been formed. In the CP group, the scaffold was completely replaced by fibrous tissue. In contrast, in the CPA-H group, new bone formation was observed around the scaffold area. The original shape of the implant scaffolds had gradually disappeared and was visible only in the center of the scaffolds (Figures 5A and 5C).

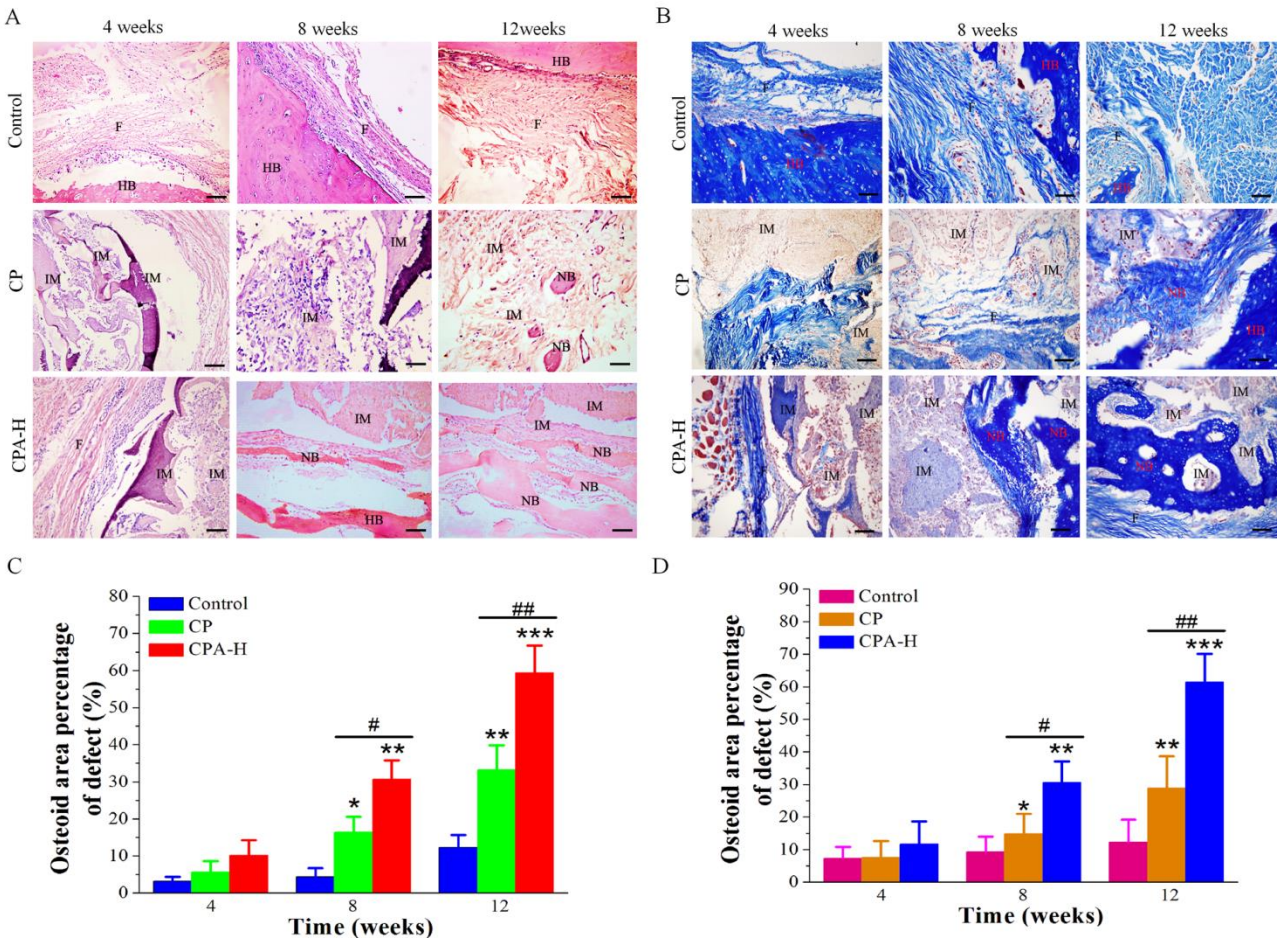

Figure 5. Histological staining of the newly formed bone 4-12 weeks after implantation of CP and CPA-H scaffolds in rabbit bone defects. (A) Hematoxylin and eosin (H&E) staining. (B) Masson staining. (C & D) show the quantitative data from (A & B), respectively. Scale bar = 100 μm. F = fibrous tissue; HB = host bone; IM = implanted material; NB = new bone. * $P < 0.05$, ** $P < 0.01$, *** $P < 0.01$, $^{\#}$ $P < 0.05$, $^{\#\#}$ $P < 0.01$.

Masson staining (Figure 5B) demonstrated that the control group had fibrous tissue at the bone defect area 4 weeks after transplantation. The fibrous tissue filled in the central portion of the defect area. On the other hand, the reconnected fibrous tissue and small areas of bone-like tissue had been found in the defect bone in the CP and CPA-H scaffold groups. In the CPA-H group, single bone fragments were observed 8 weeks after scaffold implantation. At 12 weeks, abundant new bone formation was seen in the center of the CPA-H scaffolds, but CPA-H materials had not been completely absorbed (Figures 5B and 5D).

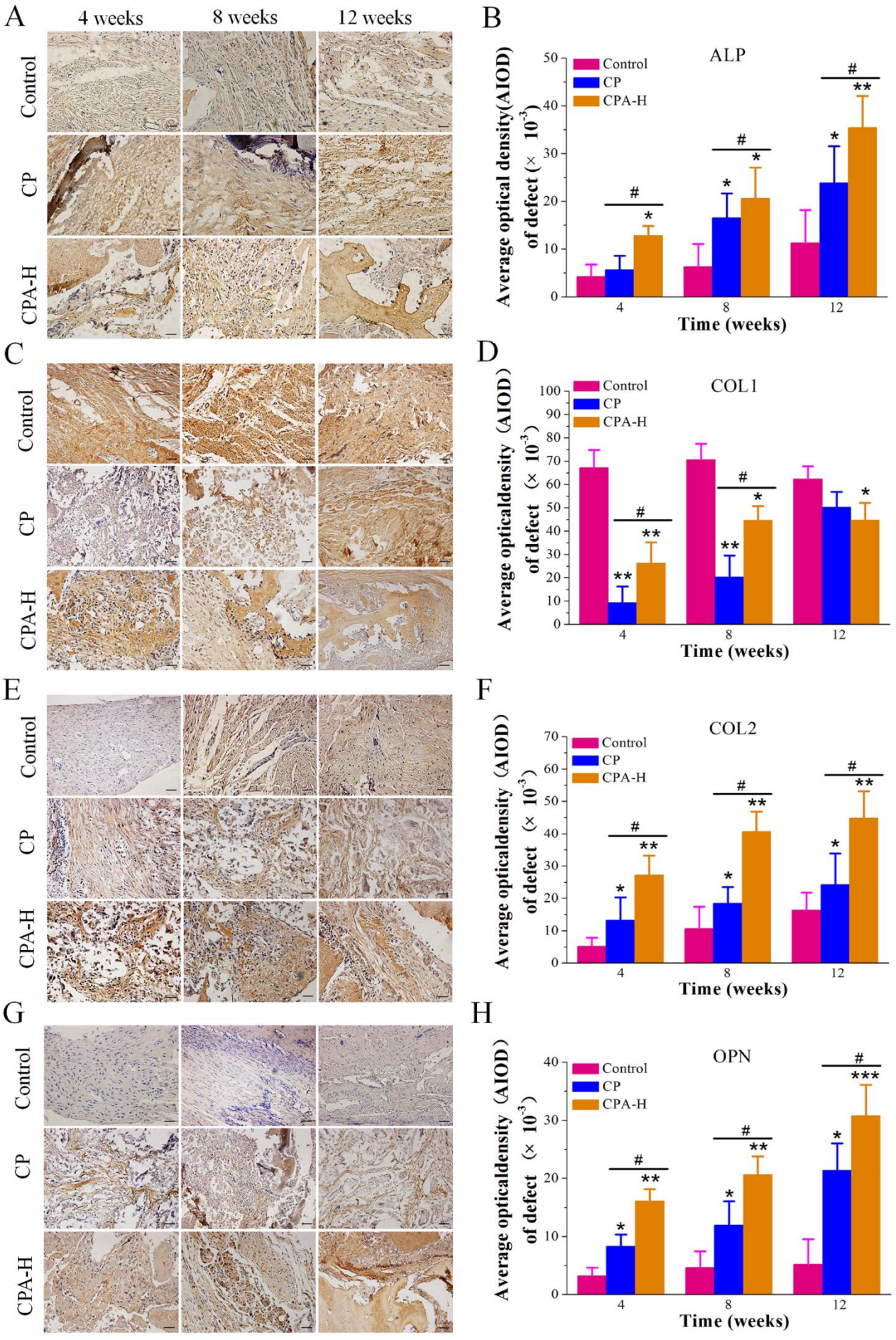
A
4 weeks
8 weeks
12 weeks
Control
CP
CPA-H
B
ALP
Control
CP
CPA-H
Average optical density(AIOD) of defect (× 10-3)
Time (weeks)
C
D
COL1
Average opticaldensity (AIOD) of defect (× 10-3)
E
F
COL2
G
H
OPN

Figure 6. Immunohistochemical staining of the newly formed bone 4-12 weeks after implantation of CP and CPA-H scaffolds in rabbit bone defects. (A, C, E and G) Immunohistochemical staining for (A) alkaline phosphatase (ALP), (C) type 1 collagen (COL1), (E) type 2 collagen (COL2), and (G) osteopontin (OPN). (B, D, F, and H) shown the quantitative data from (A, C, E and G), respectively. Data are shown as mean ± standard deviation (n = 6). Scale bar = 100 μm. * $P < 0.05$, ** $P < 0.01$, *** $P < 0.01$, $^{\#}$ $P < 0.05$, $^{\#\#}$ $P < 0.01$.

3.7 Immunohistochemical Assessment

The data of immunohistochemical assessment are shown in Figure 6. Four weeks after implantation, positive expression of ALP, COL1, COL2, and OPN was observed in all three groups. For ALP, COL2 and OPN, the expression levels showed the time and ATP dose dependent effects for all three groups, while the expression levels in CPA-H scaffolds were higher than that in CP scaffolds and control group. For COL1, high expression was observed in control group. The level of expression was found similar between 4-12 weeks. In CP group, COL1 expression increased with time, while in CPA-H group, COL1 expression increased with time and leveled off at week 12. The high expression of COL1 in control demonstrated the presence of cartilage tissue within the control group, indicating that the bone regeneration was not good. The intensity of positive staining for ALP, COL1 COL2 and OPN in the CPA-H scaffolds increased over time. This expression was mainly seen in the border of the new bone. The results demonstrate that in the control group the new tissue formed was mainly fibrous tissue containing a lot of collagen type 1. While in the CP and CPA-H groups, new bone tissues were formed and the amount of new bone in CPA-H group was much higher than that in CP group.

4. DISCUSSION

In this work, we investigated the bone regeneration efficacy of the CPA composite scaffolds for segmental bone defect healing. Our results show that the water absorption, porosity, contact angle, and degradation of the scaffolds were improved with increasing ATP content. Pore sizes are important for BTE scaffolds and has been shown to affect the progression of osteogenesis[47]. Small pore sizes (< 100 μm) not only reduce cell migration but also restrict nutrient delivery and waste removal. Additionally, it also limit the amount of new tissue regeneration[47]. It has been reported that pore sizes > 100 μm with gradients are recommended[2, 48]. In our study, the CP and CPA composite scaffolds were fabricated by salt-leaching method. The scaffolds showed porous structures, with pore sizes ranging from 250 to 500 μm, which were created by the sodium chloride particles. This porosity was beneficial for nutrient exchange, cell migration, and bone regeneration.

Ideally, biomaterials implants for clinical applications should match the mechanical properties of the host tissue and exhibit strong interfacial bonds with hard and/or soft tissues. However, the major disadvantages of the inorganic and organic component are their low mechanical strength and

fracture toughness, which typically restrict their use bone tissue engineering[3]. Our results showed that higher concentration of ATP also led to increased compressive strength, suggesting that increased ATP leads to improved mechanical strength. The ATP can provide both strength and bioactivity, while the collagen can add structural reinforcement, and toughness. The mechanical strength of the CPA composite scaffolds is lower than that of the natural bone. In the future, our strategies are to produce enhanced composites and use novel fabrication methods (e.g. 3D printing) to overcome this drawback.

Cytocompatibility of the biomaterials used in scaffolds plays a vital role in sustaining cell adhesion, proliferation, and differentiation and in enabling tissue regeneration after implantation[49]. In this study, the CPA scaffolds promoted colony morphology and induced cell proliferation when they were cocultured with cells for 1 to 7 days. The proliferation rate of cells on the CPA-H scaffold was significantly higher than the rate on the CPA-L and CP scaffolds after 7 days, suggesting that CPA scaffolds induce the proliferation of cells in a dose-dependent manner and the addition of ATP has significant effect to the cell growth. These results are consistent to the results reported by Wang et al.[40], who found that the doping of ATP within the PLGA nanofibers is able to induce the osteoblastic differentiation of hMSCs. Our results also demonstrate that CPA scaffold can increase the cell proliferation and promote osteoblasts related gene expression, therefore increase bone regeneration.

An immunofluorescence assay demonstrated that D1 cells was able to proliferate and migrate in the interior of the CPA scaffolds. Additionally, *in vivo* studies in a rat model demonstrated no evidence of severe immune response or fibrous capsule formation with the CPA scaffolds, suggesting good biocompatibility. The D1 cells grown on CPA scaffolds had upregulated levels of osteoblastic markers, including upregulated levels of Runx2 at day 7 and Osterix at day 21. These results suggest that D1 cells can differentiate into osteoblasts on CPA scaffolds. We also found that the expressions of COL1, ALP, OC, and OPN were significantly higher on CPA scaffolds than that on CP scaffolds, and this increased expression occurred in a dose-dependent and time-dependent manner. These *in vitro* findings suggest that CPA has strong osteoinductive properties. CPA may promote D1 cell osteoblast differentiation through several mechanisms: i), The elements from ATP (SiO_2, Al_2O_3, MgO, Fe_2O_3, H_2O^+, and H_2O^-), especially SiO_2, can induce D1 cells to differentiate into osteoblasts[1]. ii), ATP has desired physical properties, such as larger specific surface area, high viscosity, and high absorption ability, that make this mineral osteoinductive. iii), the synergistic effect between the chemical and physical properties of ATP may induce D1 cells to differentiate into osteoblasts.

During the *in vivo* bone tissues formation, the biomaterial should degrade slowly to match the perfect restoration of the bone defect[39, 50]. In the rabbit model we used in this study, a large amount of bone mass was observed in the CPA scaffold groups at weeks 8 and 12. This was especially obvious in the scaffold that contained CPA-H, in which the bone mass completely filled in the bony defect at week 12. Immunohistochemical analysis also demonstrated remarkable increase in the expression of ALP, COL1, COL2, and OPN in the CPA scaffolds versus in the CP scaffolds at weeks 8 and 12. These findings again suggest that ATP was able to induce the formation of vital bony structures. While the ATP has not yet been widely used in tissue engineering, this study opens a door for ATP

as a promising material for tissue engineering applications.

5. CONCLUSIONS

Salt leaching is an effective method of scaffold fabrication that has been used to create the macroporous scaffolds needed for bone tissue engineering[51]. In this study, we used the salt-leaching method to fabricate macro-mesoporous scaffolds containing either COL1/PCL or COL1/PCL/ATP as bone regeneration materials. We found that macropores (approximately 200-500 μm) had been created by sodium chloride in both the CP and CPA scaffolds, which is important for cell ingrowth and nutrition delivery. Cross-linking of the collagen with EDC/NHS changed the structure of the collagen, which led to changes in porosity and water absorption. Cross-linking improved the compressive strength and decreased the porosity of the CPA scaffolds. These results suggest that a cross-linked CPA scaffolds are more suitable for BTE. In conclusion, we found that CPA scaffolds prepared through a salt-leaching technique were more effective than CP scaffolds in inducing bone regeneration. These results suggest that CPA scaffolds, because of their specific physical and chemical properties, may have great potential for the induction of bone regeneration and promotion of bone repair. Further studies are needed to assess the use of these scaffolds in a clinical setting.

ACKNOWLEDGEMENTS

We gratefully acknowledge funding by the Key Project of Science and Technology of Jiansu Province (Grant BE2018644). We are also grateful for funding from the major projects of science and technology in Gansu Province (Grant 1203FKDA036) and from the National Natural Science Foundation (Grant 81871756). We thank Dr Aiqin Wang (Lanzhou Institute of Chemical Physics, Chinese Academy of Sciences) for providing the ATP materials used in this study. We gratefully acknowledge the Changzhou second People's Hospital Affiliated to Nanjing Medical University for support. We also thank Gen Li, Junjie Tang, and Jiuna Wang for their valuable contribution to this study. XZ also thanks the Jiangsu specially-appointed professor program for support.

CONFLICT OF INTEREST

The authors declare no conflict of interest.

REFERENCES

1. Gao, C.; Peng, S.; Feng, P.; Shuai, C., Bone biomaterials and interactions with stem cells. *Bone Research* **2017,** *5*, 17059.

2. Zhang, X.; Chang, W.; Lee, P.; Wang, Y.; Yang, M.; Li, J.; Kumbar, S. G.; Yu, X., Polymer-ceramic spiral structured scaffolds for bone tissue engineering: effect of hydroxyapatite composition on human fetal osteoblasts. *PloS one* **2014,** *9* (1), e85871.

3. Kaur, G.; Kumar, V.; Baino, F.; Mauro, J. C.; Pickrell, G.; Evans, I.; Bretcanu, O., Mechanical properties of

bioactive glasses, ceramics, glass-ceramics and composites: State-of-the-art review and future challenges. *Materials science & engineering. C, Materials for biological applications* **2019,** *104*, 109895.

4. Atala, A., Tissue Engineering and Regenerative Medicine Concepts for Clinical Application. *Rejuvenation Research* **2004,** *7*, 15-31.

5. Bae, H.; Chu, H.; Edalat, F.; Cha, J. M.; Sant, S.; Kashyap, A.; Ahari, A. F.; Kwon, C. H.; Nichol, J. W.; Manoucheri, S.; Zamanian, B.; Wang, Y.; Khademhosseini, A., Development of functional biomaterials with micro- and nanoscale technologies for tissue engineering and drug delivery applications. *Journal of Tissue Engineering and Regenerative Medicine* **2014,** *8* (1), 1-14.

6. Salgado, A. J.; Coutinho, O. P.; Reis, R. L., Bone tissue engineering: state of the art and future trends. *Macromolecular bioscience* **2004,** *4* (8), 743-65.

7. Pintippa, B. H.-L., Wang., collagen membranes:A Review. *J Periodontol* **2001,** *72*, 215-229.

8. Chia, H. N.; Wu, B. M., Recent advances in 3D printing of biomaterials. *J Biol Eng* **2015,** *9*, 4.

9. Jakobsson, A.; Ottosson, M.; Zalis, M. C.; O'Carroll, D.; Johansson, U. E.; Johansson, F., Three-dimensional functional human neuronal networks in uncompressed low-density electrospun fiber scaffolds. *Nanomedicine* **2017,** *13* (4), 1563-1573.

10. Wang, S.; Gu, Z.; Wang, Z.; Chen, X.; Cao, L.; Cai, L.; Li, Q.; Wei, J.; Shin, J. W.; Su, J., Influences of mesoporous magnesium calcium silicate on mineralization, degradability, cell responses, curcumin release from macro-mesoporous scaffolds of gliadin based biocomposites. *Sci Rep* **2018,** *8* (1), 174.

11. Fernandez de Grado, G.; Keller, L.; Idoux-Gillet, Y.; Wagner, Q.; Musset, A.-M.; Benkirane-Jessel, N.; Bornert, F.; Offner, D., Bone substitutes: a review of their characteristics, clinical use, and perspectives for large bone defects management. *Journal of Tissue Engineering* **2018,** *9*.

12. Guo, B.; Lei, B.; Li, P.; Ma, P. X., Functionalized scaffolds to enhance tissue regeneration. *Regen Biomater* **2015,** *2* (1), 47-57.

13. Cunniffe, G. M.; Curtin, C. M.; Thompson, E. M.; Dickson, G. R.; O'Brien, F. J., Content-Dependent Osteogenic Response of Nanohydroxyapatite: An in Vitro and in Vivo Assessment within Collagen-Based Scaffolds. *ACS Appl Mater Interfaces* **2016,** *8* (36), 23477-88.

14. Xu, T.; Miszuk, J. M.; Zhao, Y.; Sun, H.; Fong, H., Electrospun polycaprolactone 3D nanofibrous scaffold with interconnected and hierarchically structured pores for bone tissue engineering. *Advanced healthcare materials* **2015,** *4* (15), 2238-46.

15. Shkarina, S.; Shkarin, R.; Weinhardt, V.; Melnik, E.; Vacun, G.; Kluger, P. J.; Loza, K.; Epple, M.; Ivlev, S. I.; Baumbach, T.; Surmeneva, M. A.; Surmenev, R. A., 3D biodegradable scaffolds of polycaprolactone with silicate-containing hydroxyapatite microparticles for bone tissue engineering: high-resolution tomography and in vitro study. *Sci Rep* **2018,** *8* (1), 8907.

16. Clarke, B., Normal bone anatomy and physiology. *Clinical journal of the American Society of Nephrology : CJASN* **2008,** *3 Suppl 3*, S131-9.

17. Murugan, R.; Ramakrishna, S., Bioresorbable composite bone paste using polysaccharide based nano hydroxyapatite. *Biomaterials* **2004,** *25* (17), 3829-35.

18. Causa, F.; Netti, P. A.; Ambrosio, L.; Ciapetti, G.; Baldini, N.; Pagani, S.; Martini, D.; Giunti, A., Poly-epsilon-caprolactone/hydroxyapatite composites for bone regeneration: in vitro characterization and human osteoblast response. *J Biomed Mater Res A* **2006,** *76* (1), 151-62.

19. Jayabalan, M.; Shalumon, K. T.; Mitha, M. K.; Ganesan, K.; Epple, M., Effect of hydroxyapatite on the biodegradation and biomechanical stability of polyester nanocomposites for orthopaedic applications. *Acta Biomater* **2010,** *6* (3), 763-75.

20. Wang, X.; Zhang, G.; Qi, F.; Cheng, Y.; Lu, X.; Wang, L.; Zhao, J.; Zhao, B., Enhanced bone regeneration using an insulin-loaded nano-hydroxyapatite/collagen/PLGA composite scaffold. *Int J Nanomedicine* **2018,** *13*, 117-127.

21. Xie, C.; Lu, H.; Li, W.; Chen, F. M.; Zhao, Y. M., The use of calcium phosphate-based biomaterials in implant

dentistry. *J Mater Sci Mater Med* **2012,** *23* (3), 853-62.

22. Kumar, A.; Kargozar, S.; Baino, F.; Han, S. S., Additive Manufacturing Methods for Producing Hydroxyapatite and Hydroxyapatite-Based Composite Scaffolds: A Review. *Frontiers in Materials* **2019,** *6*, 313.

23. Yoshimoto, H.; Shin, Y. M.; Terai, H.; Vacanti, J. P., A biodegradable nanofiber scaffold by electrospinning and its potential for bone tissue engineering. *Biomaterials* **2003,** *24* (12), 2077-2082.

24. Sawyer, A. A.; Song, S. J.; Susanto, E.; Chuan, P.; Lam, C. X. F.; Woodruff, M. A.; Hutmacher, D. W.; Cool, S. M., The stimulation of healing within a rat calvarial defect by mPCL–TCP/collagen scaffolds loaded with rhBMP-2. *Biomaterials* **2009,** *30* (13), 2479-2488.

25. Wojtowicz, A. M.; Shekaran, A.; Oest, M. E.; Dupont, K. M.; Templeman, K. L.; Hutmacher, D. W.; Guldberg, R. E.; García, A. J., Coating of biomaterial scaffolds with the collagen-mimetic peptide GFOGER for bone defect repair. *Biomaterials* **2010,** *31* (9), 2574-2582.

26. Wang, C.; Zhao, Q.; Wang, M., Cryogenic 3D printing for producing hierarchical porous and rhBMP-2-loaded Ca-P/PLLA nanocomposite scaffolds for bone tissue engineering. *Biofabrication* **2017,** *9* (2), 025031.

27. Cao, H.; Kuboyama, N., A biodegradable porous composite scaffold of PGA/beta-TCP for bone tissue engineering. *Bone* **2010,** *46* (2), 386-95.

28. Yao, Q.; Cosme, J. G.; Xu, T.; Miszuk, J. M.; Picciani, P. H.; Fong, H.; Sun, H., Three dimensional electrospun PCL/PLA blend nanofibrous scaffolds with significantly improved stem cells osteogenic differentiation and cranial bone formation. *Biomaterials* **2017,** *115*, 115-127.

29. Lai, Y.; Li, Y.; Cao, H.; Long, J.; Wang, X.; Li, L.; Li, C.; Jia, Q.; Teng, B.; Tang, T.; Peng, J.; Eglin, D.; Alini, M.; Grijpma, D. W.; Richards, G.; Qin, L., Osteogenic magnesium incorporated into PLGA/TCP porous scaffold by 3D printing for repairing challenging bone defect. *Biomaterials* **2019,** *197*, 207-219.

30. Gentile, P.; Chiono, V.; Carmagnola, I.; Hatton, P. V., An overview of poly(lactic-co-glycolic) acid (PLGA)-based biomaterials for bone tissue engineering. *Int J Mol Sci* **2014,** *15* (3), 3640-59.

31. Thein-Han, W. W.; Misra, R. D., Biomimetic chitosan-nanohydroxyapatite composite scaffolds for bone tissue engineering. *Acta Biomater* **2009,** *5* (4), 1182-97.

32. Heydari, Z.; Mohebbi-Kalhori, D.; Afarani, M. S., Engineered electrospun polycaprolactone (PCL)/octacalcium phosphate (OCP) scaffold for bone tissue engineering. *Mater Sci Eng C Mater Biol Appl* **2017,** *81*, 127-132.

33. Luo, W.; Zhang, S.; Lan, Y.; Huang, C.; Wang, C.; Lai, X.; Chen, H.; Ao, N., 3D printed porous polycaprolactone/oyster shell powder (PCL/OSP) scaffolds for bone tissue engineering. *Materials Research Express* **2018,** *5* (4).

34. Baia, L. V.; Souza, W. C.; de Souza, R. J. F.; Veloso, C. O.; Chiaro, S. S. X.; Figueiredo, M. A. G., Removal of Sulfur and Nitrogen Compounds from Diesel Oil by Adsorption Using Clays as Adsorbents. *Energy & Fuels* **2017,** *31* (11), 11731-11742.

35. Zhou, X.; Huang, X.; Xie, A.; Luo, S.; Yao, C.; Li, X.; Zuo, S., V2O5-decorated Mn-Fe/attapulgite catalyst with high SO2 tolerance for SCR of NOx with NH3 at low temperature. *Chemical Engineering Journal* **2017,** *326*, 1074-1085.

36. Li, X.; Zhu, W.; Lu, X.; Zuo, S.; Yao, C.; Ni, C., Integrated nanostructures of CeO2/attapulgite/g-C3N4 as efficient catalyst for photocatalytic desulfurization: Mechanism, kinetics and influencing factors. *Chemical Engineering Journal* **2017,** *326*, 87-98.

37. Fu, M.; Li, X.; Jiang, R.; Zhang, Z., One-dimensional magnetic nanocomposites with attapulgites as templates: Growth, formation mechanism and magnetic alignment. *Applied Surface Science* **2018,** *441*, 239-250.

38. Xie, X.; Pei, F.; Wang, H.; Tan, Z.; Yang, Z.; Kang, P., Icariin: A promising osteoinductive compound for repairing bone defect and osteonecrosis. *J Biomater Appl* **2015,** *30* (3), 290-9.

39. Vashisth, P.; Bellare, J. R., Development of hybrid scaffold with biomimetic 3D architecture for bone regeneration. *Nanomedicine* **2018,** *14* (4), 1325-1336.

40. Wang, Z.; Zhao, Y.; Luo, Y.; Wang, S.; Shen, M.; Tomás, H.; Zhu, M.; Shi, X., Attapulgite-doped electrospun poly(lactic-co-glycolic acid) nanofibers enable enhanced osteogenic differentiation of human mesenchymal

stem cells. *RSC Advances* **2015,** *5* (4), 2383-2391.

41. Ruderman, G.; Mogilner, I. G.; Tolosa, E. J.; Massa, N.; Garavaglia, M.; Grigera, J. R., Ordered collagen membranes: production and characterization. *J Biomater Sci Polym Ed* **2012,** *23* (6), 823-32.

42. Sanz, M.; Lorenzo, R.; Aranda, J. J.; Martin, C.; Orsini, M., Clinical evaluation of a new collagen matrix (Mucograft prototype) to enhance the width of keratinized tissue in patients with fixed prosthetic restorations: a randomized prospective clinical trial. *J Clin Periodontol* **2009,** *36* (10), 868-76.

43. Kim, C. S.; Jung, K. H.; Kim, H.; Kim, C. B.; Kang, I. K., Collagen-grafted porous HDPE/PEAA scaffolds for bone reconstruction. *Biomater Res* **2016,** *20*, 23.

44. Cortizo, A. M.; Ruderman, G.; Mazzini, F. N.; Molinuevo, M. S.; Mogilner, I. G., Novel Vanadium-Loaded Ordered Collagen Scaffold Promotes Osteochondral Differentiation of Bone Marrow Progenitor Cells. *Int J Biomater* **2016,** *2016*, 1486350.

45. Sadiasa, A.; Nguyen, T. H.; Lee, B. T., In vitro and in vivo evaluation of porous PCL-PLLA 3D polymer scaffolds fabricated via salt leaching method for bone tissue engineering applications. *Journal of biomaterials science. Polymer edition* **2014,** *25* (2), 150-67.

46. Livak, K. J.; Schmittgen, T. D., Analysis of relative gene expression data using real-time quantitative PCR and the 2(-Delta Delta C(T)) Method. *Methods* **2001,** *25* (4), 402-8.

47. Karageorgiou, V.; Kaplan, D., Porosity of 3D biomaterial scaffolds and osteogenesis. *Biomaterials* **2005,** *26* (27), 5474-91.

48. Song, W.; Yu, X.; Markel, D. C.; Shi, T.; Ren, W., Coaxial PCL/PVA electrospun nanofibers: osseointegration enhancer and controlled drug release device. *Biofabrication* **2013,** *5* (3), 035006.

49. Keller, L.; Regiel-Futyra, A.; Gimeno, M.; Eap, S.; Mendoza, G.; Andreu, V.; Wagner, Q.; Kyziol, A.; Sebastian, V.; Stochel, G.; Arruebo, M.; Benkirane-Jessel, N., Chitosan-based nanocomposites for the repair of bone defects. *Nanomedicine* **2017,** *13* (7), 2231-2240.

50. Inzana, J. A.; Olvera, D.; Fuller, S. M.; Kelly, J. P.; Graeve, O. A.; Schwarz, E. M.; Kates, S. L.; Awad, H. A., 3D printing of composite calcium phosphate and collagen scaffolds for bone regeneration. *Biomaterials* **2014,** *35* (13), 4026-34.

51. Xie, Y.; Lan, X. R.; Bao, R. Y.; Lei, Y.; Cao, Z. Q.; Yang, M. B.; Yang, W.; Wang, Y. B., High-performance porous polylactide stereocomplex crystallite scaffolds prepared by solution blending and salt leaching. *Mater Sci Eng C Mater Biol Appl* **2018,** *90*, 602-609.